active galaxies such as NGC4261 using the Hubble Space Telescope[25]. We have applied an axisymmetric torus model with a circular cross-section to the EVN data, in order to determine the structural boundaries in the nuclear region. The compact molecular structure surrounding the nucleus is misaligned with the large-scale molecular disk of the galaxy by 34°. The radius of the inner cavity of the torus would be about 30 pc, as suggested by the location of the northwestern interaction region. The outer edge of the torus spans a diameter of 200 pc, which is based on the 4-mJy contours of the diffuse radio emission[20] and on far-infrared blackbody estimates[19]. This region also serves as a radio background for the OH amplification process. These parameters result in a torus structure with a radius of 65 pc and a thickness of 70 pc, which accounts for an obscuration angle of 60° centred on the plane of the torus and which is representative of values found for other galaxies[26]. The orientation and the shape of the extended radio contours and the symmetry axis of the velocity field indicate that the torus is tilted upward from the line of sight by 56°, and is rotated anticlockwise by 35°. This inferred model for the torus is shown as a wire-structure representation in Fig. 3c. The nuclear radiation cones with opening angles of 60°, assumed to be similar to those seen[27] in M87, represent the directions with an unobscured view of the nucleus. The radio outflow follows a twisted path within these cones, starting at the nucleus (at PA = 65°) and ending up as a double source aligned with the symmetry axis of the outer disk (at PA = 8°)[14,15]. As a result, this parameterization indicates that the nuclear accretion disk, which collimates the jet outflow inside the central cavity, is actually misaligned by 30° with the plane of the molecular torus.

In reality, the proposed torus structure does not need to have a circular cross-section. In addition, it will most probably be wrapped inside a cocoon-like surface region with a higher temperature, and will have the same outer extent of 460 pc as the diffuse radio emission and the H I absorbing gas[20]. However, the representation of the inner part of this rotating, dusty and molecular torus in Mrk231 is consistent with (all) current models of galactic nuclei and theoretical investigations[3], and supports the unification schemes for AGN. Whether a different orientation of the torus and the nuclear accretion disk represents a special case or is a general characteristic of active nuclei needs to be investigated with VLBI observations of other megamaser galaxies hosting a similar nuclear power source. □

Received 22 July; accepted 17 December 2002; doi:10.1038/nature01381.

1. Rees, M. J. Black hole models for active galactic nuclei. *Annu. Rev. Astron. Astrophys.* **22,** 471–506 (1984).
2. Krolik, J. H. & Begelman, M. C. Molecular tori in Seyfert galaxies: Feeding the monster and hiding it. *Astrophys. J.* **329,** 702–711 (1988).
3. Krolik, J. H. *Active Galactic Nuclei* (Princeton Series in Astrophysics, Princeton Univ. Press, Princeton, New Jersey, 1999).
4. Greenhill, L. J. *et al.* Detection of a subparsec diameter disk in the nucleus of NGC 4258. *Astrophys. J.* **440,** 619–627 (1995).
5. Gallimore, J. F., Baum, S. F. & O'Dea, C. P. A direct image of the obscuring disk surrounding an active galactic nucleus. *Nature* **388,** 852–854 (1997).
6. Baan, W. A. Powerful extragalactic masers. *Nature* **315,** 26–31 (1985).
7. Maloney, P. R. Powerful water masers in active galactic nuclei. *Publ. Astron. Soc. Pacif.* **19,** 401–421 (2002).
8. Herrnstein, J. R. *et al.* Polarimetric observations of the masers in NGC 4258: an upper limit on the large-scale magnetic field 0.2 parsecs from the central engine. *Astrophys. J.* **508,** 243–247 (1998).
9. Diamond, P. J., Lonsdale, Co. J., Lonsdale, Ca. J. & Smith, H. E. Global VLBI observations of the compact OH megamaser emission from III ZW 35 and IRAS 17208-0014. *Astrophys. J.* **511,** 178–184 (1999).
10. Lonsdale, Co. J., Lonsdale, Ca. J., Diamond, P. J. & Smith, H. E. Symmetric parsec-scale OH megamaser structures in Arp 220. *Astrophys. J.* **507,** 615–654 (1998).
11. Pihlström, Y. M., Conway, J. E., Booth, R. S., Diamond, P. J. & Polatidis, A. G. EVN and MERLIN observation of III Zw 35. *Astron. Astrophys.* **377,** 377–413 (2001).
12. Baan, W. A. Infrared properties of OH galaxies. *Astrophys. J.* **338,** 804–811 (1989).
13. Baan, W. A., Salzer, J. J. & LeWinter, D. Optical classification of megamaser galaxies. *Astrophys. J.* **509,** 633–645 (1998).
14. Ulvestad, J. S. *et al.* Subrelativistic radio jets and parsec-scale absorption in two Seyfert galaxies. *Astrophys. J.* **517,** L81–L84 (1999).
15. Ulvestad, J. S., Wrobel, J. M. & Carilli, C. L. Radio continuum evidence for outflow and absorption in the Seyfert 1 galaxy Markarian 231. *Astrophys. J.* **516,** 127–140 (1998).
16. Richards, A. *et al.* in *Galaxies and their Constituents at Highest Angular Resolutions* (eds Schilizzi, R. T., Vogel, S. F. P. & Elvis, M. S.) 212–215 (IAU Symposium 205, Astronomical Society of the Pacific, San Francisco, 2001).
17. Taylor, G. B., Silver, C. S., Ulvestad, J. S. & Carilli, C. L. The starburst in the central kiloparsec of Markarian 231. *Astrophys. J.* **519,** 185–190 (1999).
18. Bryant, P. M. & Scoville, N. Z. High-resolution CO observations of the ultraluminous infrared galaxy Markarian 231. *Astrophys. J.* **457,** 678–692 (1996).
19. Downes, D. & Solomon, P. M. Rotating nuclear rings and extreme starbursts in ultraluminous galaxies. *Astrophys. J.* **507,** 615–654 (1998).
20. Carilli, C. L., Wrobel, J. M. & Ulvestad, J. S. A subkiloparsec disk in Markarian 231. *Astron. J.* **115,** 928–937 (1998).
21. Baan, W. A., Henkel, C. & Güsten, R. Rotationally excited OH in megamaser galaxies. *Astron. Astrophys.* **185,** 14–24 (1987).
22. Randell, J., Field, D., Jones, K. N., Yates, J. A. & Gray, M. D. The OH zone in OH megamaser galaxies. *Astron. Astrophys.* **300,** 659–674 (1995).
23. Baan, W. A., Wood, P. A. D. & Haschick, A. D. Broad hydroxyl emission in IC 4553. *Astrophys. J.* **260,** L49–L52 (1982).
24. Keiichi, W. & Norman, C. A. Obscuring material around Seyfert nuclei with starbursts. *Astrophys. J.* **566,** L21–L24 (2002).
25. v. Langevelde, H. *et al.* A thin circumnuclear disk in NGC 4261. *Astron. Astrophys.* **354,** L45–L48 (2000).
26. Schmitt, H. R. *et al.* Testing the unified model with a infrared-selected sample of Seyfert galaxies. *Astrophys. J.* **555,** 663–672 (2001).
27. William, J., Biretta, J. A. & Livio, M. Formation of the radio jet in M87 at 100 Schwarzschild radii from the central black hole. *Nature* **401,** 891–892 (1999).

Acknowledgements We thank C. Carilli for providing a map of the diffuse continuum structure in Mrk231. H.-R.K. thanks O. Möller for advice on programming in OpenGL software. The European VLBI Network is a joint facility of European, Chinese, South African and other radio astronomy institutes funded by their national research councils. The Westerbork Synthesis Radio Telescope is operated by ASTRON (Netherlands Foundation for Research in Astronomy) with support from the Netherlands Foundation for Scientific Research (NWO).

Competing interests statement The authors declare that they have no competing financial interests.

Correspondence and requests for materials should be addressed to H.-R.K. (e-mail: hrkloeck@astro.rug.nl).

Quantum oscillations in two coupled charge qubits

Yu. A. Pashkin*†, T. Yamamoto*‡, O. Astafiev*, Y. Nakamura*‡, D. V. Averin§ & J. S. Tsai*‡

* *The Institute of Physical and Chemical Research (RIKEN), Wako, Saitama 351-0198, Japan*
‡ *NEC Fundamental Research Laboratories, Tsukuba, Ibaraki 305-8501, Japan*
§ *Department of Physics and Astronomy, SUNY Stony Brook, New York 11794-3800, USA*

A practical quantum computer[1], if built, would consist of a set of coupled two-level quantum systems (qubits). Among the variety of qubits implemented[2], solid-state qubits are of particular interest because of their potential suitability for integrated devices. A variety of qubits based on Josephson junctions[3,4] have been implemented[5–8]; these exploit the coherence of Cooper-pair tunnelling in the superconducting state[5–10]. Despite apparent progress in the implementation of individual solid-state qubits, there have been no experimental reports of multiple qubit gates—a basic requirement for building a real quantum computer. Here we demonstrate a Josephson circuit consisting of two coupled charge qubits. Using a pulse technique, we coherently mix quantum states and observe quantum oscillations, the spectrum of which reflects interaction between the qubits. Our results demonstrate the feasibility of coupling multiple solid-state qubits, and indicate the existence of entangled two-qubit states.

One of the physical realizations of a solid-state qubit is provided

† Permanent address: Lebedev Physical Institute, Moscow 117924, Russia.

by a Cooper-pair box[11]. The two charge states of the box, say $|0\rangle$ and $|1\rangle$, differing by one Cooper pair are coherently mixed by the Josephson coupling, as has been confirmed experimentally[12,13]. Quantum state manipulation of such a system can be done by using a non-adiabatic pulse technique, and read-out can be performed by a properly biased probe electrode[5]. Here we take one step further on the way to implementation of quantum logic gates by integrating two charge qubits and demonstrating their interaction.

The two charge qubits of our circuit are electrostatically coupled by an on-chip capacitor (Fig. 1). The right qubit has a SQUID (superconducting quantum interference device) geometry to allow control of the Josephson coupling to its reservoir. Both qubits have a common pulse gate but separate d.c. gates, probes and reservoirs. The pulse gate has nominally equal coupling to each box. The hamiltonian of the system in the two-qubit charge basis $|00\rangle$, $|10\rangle$, $|01\rangle$ and $|11\rangle$ reads:

$$H = \begin{bmatrix} E_{00} & -\frac{1}{2}E_{J1} & -\frac{1}{2}E_{J2} & 0 \\ -\frac{1}{2}E_{J1} & E_{10} & 0 & -\frac{1}{2}E_{J2} \\ -\frac{1}{2}E_{J2} & 0 & E_{01} & -\frac{1}{2}E_{J1} \\ 0 & -\frac{1}{2}E_{J2} & -\frac{1}{2}E_{J1} & E_{11} \end{bmatrix} \quad (1)$$

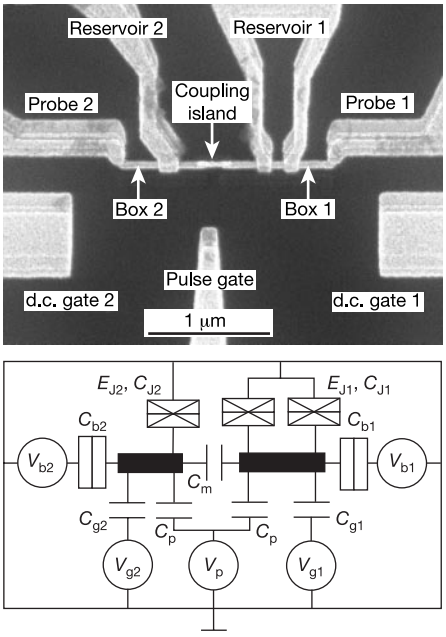

Figure 1 Two capacitively coupled charge qubits. **a**, Scanning electron micrograph of the sample. The qubits were fabricated by electron-beam lithography and three-angle evaporation of Al (light areas) on a SiN_x insulating layer (dark) (see ref. 5 for fabrication details). Two qubits are coupled by an additional coupling island overlapping both Cooper-pair boxes. Although the coupling island has a finite tunnelling resistance (~10 MΩ) to the boxes, we consider the coupling as purely capacitive (represented by a single capacitor in the equivalent circuit) because all the tunnelling processes are completely blocked. The estimated capacitance of the island to the ground is ~1 aF. **b**, Equivalent circuit of the device. The parameters (see text for definitions) obtained from the d.c. measurements are: $C_{J1} = 620$ aF, $C_{J2} = 460$ aF, $C_{b1} = 41$ aF, $C_{b2} = 50$ aF, $C_{g1} = 0.60$ aF, $C_{g2} = 0.61$ aF, $C_p \approx 1$ aF and $C_m = 34$ aF, and the corresponding energies are $E_{c1} = 484\,\mu$eV (117 GHz in frequency units), $E_{c2} = 628\,\mu$eV (152 GHz) and $E_m = 65\,\mu$eV (15.7 GHz). Josephson coupling energies, $E_{J1} = 55\,\mu$eV (13.4 GHz) and $E_{J2} = 38\,\mu$eV (9.1 GHz), were determined from the single qubit measurements described in the text. Probe junction tunnel resistance is equal to 31.6 MΩ (left) and 34.5 MΩ (right). Superconducting energy gap is 210 μeV. Black bars denote Cooper-pair boxes. Vertical rectangles containing a single line represent tunnel junctions without Josephson coupling; horizontal, crossed rectangles represent Josephson tunnel junctions.

where $E_{n1n2} = E_{c1}(n_{g1} - n_1)^2 + E_{c2}(n_{g2} - n_2)^2 + E_m(n_{g1} - n_1)\times(n_{g2} - n_2)$ is the total electrostatic energy of the system (n_1, $n_2 = 0, 1$ is the number of excess Cooper pairs in the first and the second box), $E_{J1}(E_{J2})$ is the Josephson coupling energy of the first (second) box and the reservoir, $E_{c1,2} = 4e^2C_{\Sigma2,1}/2(C_{\Sigma1}C_{\Sigma2} - C_m^2)$ are the effective Cooper-pair charging energies, and e is the charge on the electron, $C_{\Sigma1,2}$ are the sum of all capacitances connected to the corresponding island including the coupling capacitance C_m and $n_{g1,2} = (C_{g1,2}V_{g1,2} + C_pV_p)/2e$ are the normalized charges induced on the corresponding qubit by the d.c. and pulse gate electrodes. The coupling energy E_m depends not only on C_m, but also on the total capacitance of the boxes: $E_m = 4e^2C_m/(C_{\Sigma1}C_{\Sigma2} - C_m^2)$. Application of gate voltages allows us to control diagonal elements of the hamiltonian of equation (1). The circuit was fabricated to have the following relation between the characteristic energies: $E_{J1,2} \approx E_m < E_{c1,2}$. This ensures coherent superposition of the four charge states $|00\rangle$, $|01\rangle$, $|10\rangle$ and $|11\rangle$ around $n_{g1} = n_{g2} = 0.5$, while other charge states are separated by large energy gaps. The above condition justifies the use of a four-level approximation for the description of the system. In our notation $|n_1n_2\rangle$ of the charge states used throughout the text, n_1 and n_2 refer to the number of excess Cooper pairs in the first and the second qubits, respectively.

In the absence of Josephson coupling, the ground-state charging diagram (n_1, n_2) (ref. 14; Fig. 2a) consists of hexagonal cells whose boundaries delimit two neighbouring charge states with degenerate electrostatic energies. For example, points R and L in Fig. 2a

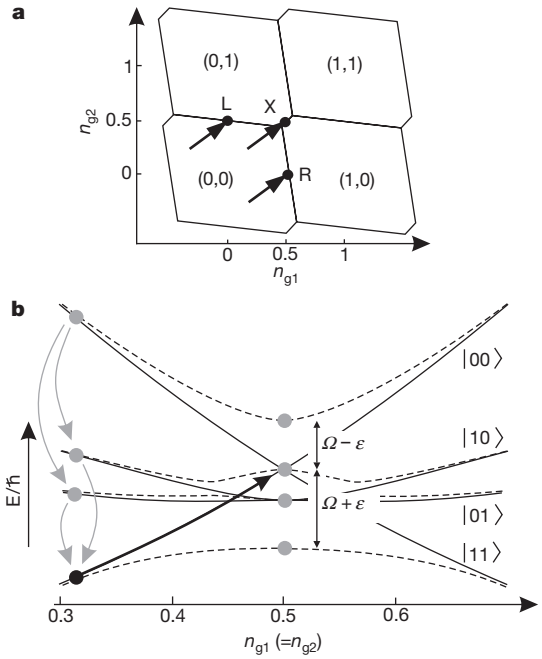

Figure 2 Pulse operation of device. **a**, Ground-state charging diagram of the coupled qubits as a function of the normalized gate charges n_{g1} and n_{g2}. The number of Cooper pairs n_1 and n_2 in the neighbouring cells differs by one. The electrostatic energies E_{n1n2} are degenerate at the boundaries. Points R and L correspond to energy degeneracy in the first and the second qubit, respectively. Point X is doubly degenerate: $E_{00} = E_{11}$ and $E_{10} = E_{01}$. Arrows show how pulses shift the system in the experiment. **b**, Energy diagram of the system along the line $n_{g1} = n_{g2}$. Solid lines are the electrostatic energies of the charge states $|00\rangle$, $|10\rangle$, $|01\rangle$ and $|11\rangle$. Dashed lines are eigenenergies of the hamiltonian equation (1). Far from co-resonance (point X in **a**), the system stays in $|00\rangle$. After the pulse brings the system to the co-resonance (solid arrow), the system starts to evolve producing a superposed state $|\psi(t)\rangle = c_1|00\rangle + c_2|10\rangle + c_3|01\rangle + c_4|11\rangle$. The amplitudes $|c_i|$ ($i = 1, 2, 3, 4$) remain 'frozen' after the pulse termination until the resulting state decays into the ground state. The decay process indicated by grey arrows contributes to the probe currents proportional to the probabilities, equation (3).

correspond to a degeneracy between the states $|00\rangle$ and $|10\rangle$ and the states $|00\rangle$ and $|01\rangle$ differing by one Cooper pair in the first and the second Cooper-pair box, respectively. If we choose the d.c. gate charges n_{g1} and n_{g2} far from the boundaries but within the (0,0) cell, then because of large electrostatic energies we can assume that the system remains in the state $|00\rangle$. As the pulse gate has equal coupling to each qubit, the application of a pulse shifts the state of the system on this diagram along a line tilted at 45°, indicated by arrows in Fig. 2a. The charging diagram remains valid for small Josephson coupling except on the boundaries where charge states become superposed. When the system is driven non-adiabatically to point R or L, it behaves like a single qubit oscillating between the degenerate states with a frequency $\omega_{1,2} = E_{J1,2}/\hbar$. Applying arrays of pulses and measuring oscillations of the probe currents I_1 and I_2, we can determine the Josephson energies of each qubit. The accuracy of the measured $E_{J1,2}$ is very high, because the electrostatic coupling through C_m has almost no effect on $\omega_{1,2}$ along the boundaries in the vicinity of R and L.

At the 'co-resonance' point X($n_{g1} = n_{g2} = 0.5$), the system has a double degeneracy, $E_{00} = E_{11}$, $E_{10} = E_{01}$, and the dynamics of the quantum evolution become more complex and reflect the coupling between the qubits. The cross-section of the energy bands through point X is shown in Fig. 2b. Exactly at the co-resonance, all four charge states are mixed and the state of the system can be expressed in general as

$$|\psi(t)\rangle = c_1|00\rangle + c_2|10\rangle + c_3|01\rangle + c_4|11\rangle \quad (2)$$

where $|c_i|(i = 1, 2, 3, 4)$ are the time-dependent probability amplitudes obeying a normalization condition $\sum_{i=1}^{4} |c_i|^2 = 1$. Using the hamiltonian of equation (1) and initial conditions, we can calculate the probabilities $|c_i|^2$ of each charge state. However, in our read-out scheme, we measure a probe current $I_{1,2}$ proportional to the probability $p_{1,2}(1)$ of each qubit having a Cooper pair on it regardless of the state of the other qubit; that is, $I_1 \propto p_1(1) \equiv |c_2|^2 + |c_4|^2$ and $I_2 \propto p_2(1) \equiv |c_3|^2 + |c_4|^2$. Assuming that the initial state at $t = 0$ is $|00\rangle$, we can derive the time evolution of these probabilities for an ideal rectangular pulse shape of length Δt:

$$p_{1,2}(1) = (1/4)[2 - (1 - \chi_{1,2})\cos\{(\Omega + \varepsilon)\Delta t\} - (1 + \chi_{1,2})\cos\{(\Omega - \varepsilon)\Delta t\}] \quad (3)$$

where $\chi_{1,2} = (E_{J2,1}^2 - E_{J1,2}^2 + E_m^2/4)/(4\hbar^2\Omega\varepsilon)$, $\Omega = ((E_{J1} + E_{J2})^2 + (E_m/2)^2)^{1/2}/2\hbar$, $\varepsilon = ((E_{J1} - E_{J2})^2 + (E_m/2)^2)^{1/2}/2\hbar$.

Unlike the single qubit case, there are two frequencies present in the oscillation spectrum of the qubits: $\Omega + \varepsilon$ and $\Omega - \varepsilon$, both dependent on E_{J1}, E_{J2} and E_m. We can identify these frequencies with the energy gaps in Fig. 2b. Note that in the uncoupled situation ($E_m = 0$), $\Omega \pm \varepsilon = E_{J1,2}/\hbar$ and each qubit oscillates with its own frequency $\omega_{1,2}$. We stress, however, that the above consideration is valid only in the ideal case when the pulse has zero rise/fall time, and the time evolution occurs exactly at the co-resonance point.

The idea of our experiment is shown schematically in Fig. 2b. From the state $|00\rangle$ (shown as a black dot), the pulse (solid arrow) brings the system to the co-resonance point, and the system evolves for the pulse duration time Δt, producing a superposed state equation (2) indicated by grey circles. After the pulse termination, the system remains in the superposed state until it decays (grey arrows) in the ground state by emitting quasiparticles into the probe junctions biased at $V_{b1,2} \approx 600\,\mu$eV. To accumulate a signal, a pulse array ($\sim 3 \times 10^5$ pulses) was applied to the pulse gate. The repetition time between the pulses was 64 ns, long enough (in comparison to the quasiparticle relaxation time of $\sim$10 ns) to let the system decay through a Josephson-quasiparticle cycle[15] and give rise to a probe current proportional to $p_{1,2}$. The estimated amplitude of the applied pulses is $V_p \approx 30$ mV.

The results obtained in this way are presented in Fig. 3. First, by tuning n_{g1} and n_{g2}, we do single qubit measurements by bringing

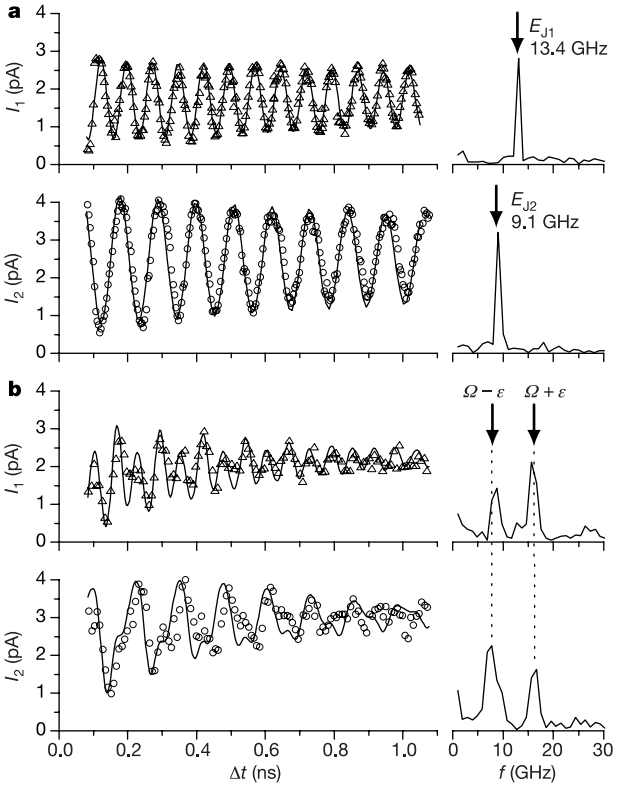

Figure 3 Quantum oscillations in qubits. **a**, Probe current oscillations in the first (top) and the second (bottom) qubit when the system is driven to the points R and L, respectively. Right panel shows corresponding spectra obtained by Fourier transform. In both cases, the experimental data (open triangles and open dots) can be fitted to a cosine dependence (solid lines) with an exponential decay with 2.5 ns time constant. **b**, Probe current oscillations in the qubits at the co-resonance point X. Their spectra (right panel) contain two components. Arrows and dotted lines indicate the position of $\Omega + \varepsilon$, $\Omega - \varepsilon$ obtained from equation (3) using $E_{J1} = 13.4$ GHz, $E_{J2} = 9.1$ GHz measured in the single qubit experiments (Fig. 3a) and $E_m = 15.7$ GHz estimated independently from d.c. measurements. Solid lines are fits obtained from numerical simulation with the parameters $E_{J1} = 13.4$ GHz, $E_{J2} = 9.1$ GHz and $E_m = 14.5$ GHz. Finite pulse rise/fall time and an initial condition that is not pure $|00\rangle$ were taken into account. The introduced exponential decay time is 0.6 ns.

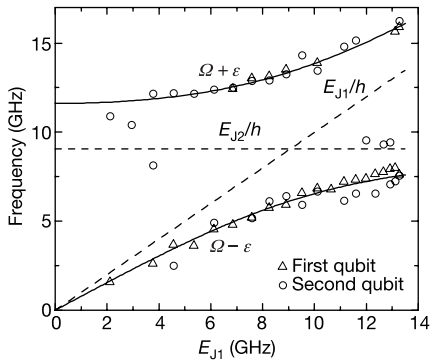

Figure 4 E_{J1} dependence of the spectrum components obtained by Fourier transform of the oscillations at the co-resonance. Open triangles and open circles show respectively frequency components measured in the first and second qubit; solid lines, dependence of $\Omega + \varepsilon$ and $\Omega - \varepsilon$ obtained from equation (3) using $E_{J2} = 9.1$ Ghz and $E_m = 14.5$ GHz and varying E_{J1} from zero up to its maximum value of 13.4 GHz; dashed lines, dependence of the oscillation frequencies of both qubits in the case of zero coupling ($E_m = 0$).

the system to point R or L and thus exciting autonomous oscillations in one of the qubits (Fig. 3a). The spectra of the oscillations can be fitted to a cosine function with an exponential decay time of about 2.5 ns. The spectra of the oscillations (right panels of Fig. 3a) obtained by Fourier transform contain one pronounced component at 13.4 GHz for the first qubit and at 9.1 GHz for the second qubit. We identify these values with E_{J1} and E_{J2}. Judging from our previous experiments (see, for example, ref. 13) we conclude that these values are close to what we expect for the given fabrication parameters (that is, overlap area and oxidation conditions). Then, by changing n_{g1} and n_{g2}, the system is driven to the co-resonance point, and the induced quantum oscillations are traced using the same technique. The oscillation pattern becomes more complex (Fig. 3b), and more frequency components appear in the spectrum. The observed spectral properties of the oscillations agree with the predictions of equation (3), in that there are two peaks in the spectrum and the peak positions are close to the expected frequencies $\Omega + \varepsilon$ and $\Omega - \varepsilon$ for the parameters $E_{J1} = 13.4\,\mathrm{GHz}$ and $E_{J2} = 9.1\,\mathrm{GHz}$ measured in the single qubit experiments (Fig. 3a), and $E_m = 15.7\,\mathrm{GHz}$ estimated from independent measurements of d.c. current–voltage–gate-voltage characteristics. The positions of the $\Omega + \varepsilon$ and $\Omega - \varepsilon$ peaks expected from equation (3) are indicated by arrows and dotted lines in Fig. 3. The decay time ($\sim$0.6 ns) of the coupled oscillations is shorter compared to the case of the independent oscillations, as is expected because an extra decoherence channel appears for each qubit after coupling it to its neighbour. However, the amplitudes of the spectral peaks do not exactly agree with equation (3). We attribute this to the non-ideal pulse shape (finite rise/fall time $\sim$35 ps), and the fact that a small shift of n_{g1} and n_{g2} off the co-resonance drastically changes the oscillation pattern. Also, even far from the co-resonance, we still have a small contribution to the initial state from charge states other than $|00\rangle$ distorting the oscillations. We have performed numerical simulations of the oscillation pattern, taking into account a realistic pulse shape and an initial condition of not pure $|00\rangle$, assuming the system is exactly at the co-resonance. The resulting fits are shown in Fig. 3b as solid lines. We found that $E_m = 14.5\,\mathrm{GHz}$, close to the value estimated from the d.c. measurements, gives better agreement of the fit with the experimental data.

Finally, we checked the dependence of the oscillation frequencies on E_{J1}, controlled by a weak magnetic field (up to 20 G). The results are shown in Fig. 4. The plot contains the data from both qubits represented by open triangles (first qubit) and open circles (second qubit). Without coupling ($E_m = 0$), the single peaks in each qubit would follow the dashed lines with an intersection at $E_{J1} = E_{J2}$. The introduced coupling modifies this dependence by creating a gap, and shifting the frequencies to higher and lower values; the spacing between the two branches is equal to $E_m/2h$ when $E_{J1} = E_{J2}$. We compare the observed dependence with the prediction of equation (3) (given by solid lines) and find a remarkable agreement.

The observed quantum coherent dynamics of coupled qubits in the vicinity of the co-resonance (in particular, the double-frequency structure of the probability oscillations in both qubits, and frequency 'repulsion' at $E_{J1} \approx E_{J2}$—see Figs 3b and 4) indicates that the two qubits become entangled during the course of coupled oscillations, although direct measurement of the degree of entanglement was not possible. Simple calculations based on the standard expression for the entanglement of the pure states[16] show that, with an ideal pulse shape and the $|00\rangle$ initial condition, the wavefunction shown in equation (2) evolves through a maximally entangled state in the case of equal Josephson energies. The numerical simulations confirm that the amount of entanglement does not decrease significantly when realistic experimental conditions are taken into account. The relatively large observed oscillation amplitude (about 50% of the expected value) also suggests the existence of entangled states even in our multi-pulse averaged experiment. □

Received 21 October; accepted 10 December 2002; doi:10.1038/nature01365.

1. Nielsen, M. A. & Chuang, I. L. *Quantum Computation and Quantum Information* (Cambridge Univ. Press, Cambridge, 2000).
2. Clark, R. G. (ed.) *Experimental Implementation of Quantum Computation* (Rinton, Princeton, 2001).
3. Averin, D. V. Quantum computing and quantum measurement with mesoscopic Josephson junctions. *Fortschr. Phys.* **48,** 1055–1074 (2000).
4. Makhlin, Y., Schön, G. & Shnirman, A. Quantum state engineering with Josephson-junction devices. *Rev. Mod. Phys.* **73,** 357–400 (2001).
5. Nakamura, Y., Pashkin, Yu. A. & Tsai, J. S. Coherent control of macroscopic quantum states in a single-Cooper-pair box. *Nature* **398,** 786–788 (1999).
6. Vion, D. *et al.* Manipulating the quantum state of an electrical circuit. *Science* **296,** 886–889 (2002).
7. Yu, Y., Han, S., Chu, X., Chu, S.-I. & Wang, Z. Coherent temporal oscillations of macroscopic quantum states in a Josephson junction. *Science* **296,** 889–892 (2002).
8. Martinis, J. M., Nam, S., Aumentado, J. & Urbina, C. Rabi oscillations in a large Josephson-junction qubit. *Phys. Rev. Lett* **89,** 117901 (2002).
9. Friedman, J. R., Patel, V., Chen, W., Toltygo, S. K. & Lukens, J. E. Quantum superposition of distinct macroscopic states. *Nature* **406,** 43–46 (2000).
10. Van der Wal, C. H. *et al.* Quantum superposition of macroscopic persistent-current states. *Science* **290,** 773–777 (2000).
11. Bouchiat, V., Vion, D., Joyez, P., Esteve, D. & Devoret, M. H. Quantum coherence with a single Cooper pair. *Phys. Scripta T* **76,** 165–170 (1998).
12. Flees, D. J., Han, S. & Lukens, J. E. Interband transitions and band gap measurements in Bloch transistors. *Phys. Rev. Lett.* **78,** 4817–4820 (1997).
13. Nakamura, Y., Chen, C. D. & Tsai, J. S. Spectroscopy of energy-level splitting between two macroscopic quantum states of charge coherently superposed by Josephson coupling. *Phys. Rev. Lett.* **79,** 2328–2331 (1997).
14. Esteve, D. in *Single Charge Tunneling* (eds Grabert, H. & Devoret, M. H.) 109–137 (Plenum, New York, 1992).
15. Fulton, T. A., Gammel, P. L., Bishop, D. J., Dunkleberger, L. N. & Dolan, G. J. Observation of combined Josephson and charging effects in small tunnel junction circuits. *Phys. Rev. Lett.* **63,** 1307–1310 (1989).
16. Bennett, C. H., Bernstein, H. J., Popescu, S. & Schumacher, B. Concentrating partial entanglement by local operations. *Phys. Rev. A* **53,** 2046–2052 (1996).

Acknowledgements We thank B. L. Altshuler, X. D. Hu, H. Im, S. Ishizaka, F. Nori, T. Sakamoto and J. Q. You for discussions. D.V.A. was supported by AFORS, and by NSA and ARDA under an ARO contract.

Competing interests statement The authors declare that they have no competing financial interests.

Correspondence and requests for materials should be addressed to J.S.T. (e-mail: tsai@frl.cl.nec.co.jp).

Probing molecular dynamics with attosecond resolution using correlated wave packet pairs

Hiromichi Niikura*, F. Légaré*†, R. Hasbani*, Misha Yu Ivanov*, D. M. Villeneuve* & P. B. Corkum*

** National Research Council of Canada, 100 Sussex Drive, Ottawa, Ontario K1A 0R6, Canada*
† Université de Sherbrooke, Sherbrooke PQ, Canada

Spectroscopic measurements with increasingly higher time resolution are generally thought to require increasingly shorter laser pulses, as illustrated by the recent monitoring of the decay of core-excited krypton[1] using attosecond photon pulses[2,3]. However, an alternative approach to probing ultrafast dynamic processes might be provided by entanglement, which has improved the precision[4,5] of quantum optical measurements. Here we use this approach to observe the motion of a D_2^+ vibrational wave packet formed during the multiphoton ionization of D_2 over several femtoseconds with a precision of about 200 attoseconds and 0.05 ångströms, by exploiting the correlation between the electronic and nuclear wave packets formed during the ionization event. An intense infrared laser field drives the electron wave packet, and electron recollision[6–11] probes the nuclear motion. Our results show that laser pulse duration need